OPEN ACCESS
IOP Publishing
Modelling and Simulation in Materials Science and Engineering
Modelling Simul. Mater. Sci. Eng. **31** (2023) 075008 (17pp) https://doi.org/10.1088/1361-651X/acf060

A molecular dynamics study of the effects of velocity and diameter on the impact behavior of zinc oxide nanoparticles

Scott Burlison[1,2], **Michael F Becker**[2,3,4] **and Desiderio Kovar**[1,2,3,*]

[1] Department of Mechanical Engineering, University of Texas at Austin, Austin, TX 78712, United States of America
[2] Center for Additive Manufacturing and Design Innovation, University of Texas at Austin, Austin, TX 78712, United States of America
[3] Materials Science and Engineering Program, University of Texas at Austin, Austin, TX 78712, United States of America
[4] Department of Electrical and Computer Engineering, University of Texas at Austin, Austin, TX 78712, United States of America

E-mail: dekovar@austin.utexas.edu

Received 17 May 2023; revised 8 August 2023
Accepted for publication 15 August 2023
Published 1 September 2023

Abstract

Molecular dynamics simulations of particle impact have been conducted for a ceramic with mixed ionic-covalent bonding. For these simulations, individual zinc oxide (ZnO) nanoparticles (NPs) were impacted onto a ZnO substrate to observe the effects of impact velocity (1500–3500 m s^{-1}) and particle diameter (10, 20, and 30 nm) on particle deformation and film formation mechanisms that arise during the micro-cold spray process for producing films. The study shows that a critical impact velocity range exists, generally between 1500 and 3000 m s^{-1}, for sticking of the NP to the substrate. Results suggest that solid-state amorphization-induced viscous flow is the primary deformation mechanism present during impact. Decreasing particle diameter and increasing impact velocity results in an increased degree of amorphization and higher

* Author to whom any correspondence should be addressed.

local temperatures within the particle. The impact behavior of mixed ionic-covalent bonded ZnO is compared to the behavior of previously studied ionic and covalent materials.

Keywords: molecular dynamics, nanoparticle, impaction, zinc oxide, micro-cold spray

(Some figures may appear in colour only in the online journal)

1. Introduction

Micro-cold spray (MCS) is one of several related aerosol deposition processes that produces thick films at room temperature from a solid particle aerosol. MCS (McCallister *et al* 2021), the laser ablation of microparticle aerosol process (Ma *et al* 2010), and low-pressure cold spray (Gibas *et al* 2023) produce films by impacting nm- to μm-scale particles onto a substrate at high velocities. The particles are accelerated through a nozzle by means of a pressure differential of near atmosphere upstream of the nozzle entrance to low vacuum at the outlet of the nozzle. Many ceramics and some metals have been successfully deposited through these aerosol processes, including alumina (Akedo 2006, 2008, Exner *et al* 2021), tin dioxide (Hanft *et al* 2018, Gibas *et al* 2023), yttria-stabilized zirconia (Song *et al* 2021), silicon carbide (Kim and Lee 2019), and silver (McCallister *et al* 2019), among others.

The current state of the art for aerosol impact process requires considerable empirical experimentation to determine conditions that produce high quality films (Hanft *et al* 2015). An understanding of the influence of processing parameters on the mechanisms that result in particle deformation and film formation for ceramic particles is therefore needed to reduce the time and expense for empirically determining an acceptable processing window for film formation. However, studying these mechanisms experimentally is challenging because particle impacts occur over a time scale of picoseconds, making it practically impossible to observe impact phenomena in real time.

Molecular dynamics (MD) simulations offer a solution because they can be used to study phenomena that occur at the time scales relevant for deformation during particle impact. This has been demonstrated using simplified particle geometries and potential functions to study the influence of process parameters on deformation and film formation mechanisms during impact of TiO_2 particles (Daneshian *et al* 2022). However, the study of underlying deformation mechanisms such as dislocation plasticity and amorphization/viscous flow requires potential functions that more accurately predict the atomic or ionic interactions that arise during deformation. Although the film formation mechanisms are sensitive to particle size, it has been shown that the same intrinsic deformation mechanisms such as dislocation motion and amorphization/viscous flow occur over a broad range of particle sizes (Moyers *et al* 2023). This suggests that MD simulations offer a means to study with reasonable computational expense underlying deformation mechanisms that arise during particle impact by using sub-100 nm particles.

Several previous MD studies have focused on high velocity impact of sub-10 nm ceramic particles that have a strongly ionic character (Ogawa 2005, 2006, Jami and Jabbarzadeh 2020, Moyers *et al* 2022). More recently, an MD study has been conducted on the particle deformation behavior of a highly covalent ceramic, SiC (Davies *et al* 2022). Comparing these studies shows that, although there are some similarities in the impact behavior of ionic ceramics and covalent ceramics, there are also some notable differences. For both classes of ceramic materials, impact normal to the substrate results in deformation by amorphization followed by viscous flow when the impact velocity exceeds a critical velocity. Below the critical velocity,

particles impact elastically and then rebound without sticking. The critical impact velocity for a fixed particle size is, however, notably higher for covalent SiC compared to the primarily ionic oxides such as ZrO_2 and Y_2O_3.

Toe *et al* have shown experimentally that it is possible to deposit the mixed ionic-covalent ceramic zinc oxide (ZnO) using MCS (2022). However, there have been no previous studies that focus on the fundamental deformation mechanisms in this class of ceramics. In this paper, we report on the deformation mechanisms present during single particle impact of ZnO nanoparticles (NPs) and study how these mechanisms are affected by particle size and particle impact velocity. We utilize MD simulations and systematically alter NP diameter (10–30 nm) and velocity (500–3500 m s^{-1}).

2. Methods

2.1. Numerical model

MD simulations of individual ZnO NPs were conducted using the open-source LAMMPS (Large-scale Atomic/Molecular Massively Parallel Simulator) software (Plimpton 1995, Thompson *et al* 2022). All simulations were conducted on the Stampede2 supercomputer at the Texas Advanced Computing Center at The University of Texas at Austin. A three-body Tersoff-style potential from Erhart was used to model atomic interactions within the ZnO NP-substrate system (Erhart *et al* 2006) and the complete model equations and parameters are given in this reference. The relevant potential was implemented in LAMMPS through OpenKIM, the Open Knowledgebase of Interatomic Models (Tadmor *et al* 2011). This potential has been vetted to accurately predict bulk properties of ZnO, including structures, cohesive energies, and elastic properties by comparison to experiments and density functional theory calculations.

Plastic properties of ZnO were not investigated by Erhart *et al* in the original paper documenting the potential. However, two subsequent studies by Gheewala (Gheewala *et al* 2009, 2010) utilized this potential for MD simulations of nanoindentation and nanoscratching. Gheewala *et al* (2009) modeled nanoindentation of pure ZnO and an Ag–ZnO coating stack through both MD and a coupled finite element/MD methodology. Gheewala (Gheewala 2010) compared MD simulations and experiments of nanoindentation and nanoscratching, in which they observed mechanical properties of films, pop-ins, and regions of plastic deformation. General agreement was found between the simulations and experiments.

2.2. Crystal structure generation

A wurtzite crystal structure was initially assigned to the ZnO lattice with a lattice parameter of 0.325 nm (Morkoç and Özgür 2009, Mulheran and Meskine 2011). The wurtzite crystal structure is composed of two overlapping hexagonal close-packed sublattices, with one sublattice containing Zn atoms and the other containing O atoms that are vertically offset by 0.375 in fractional coordinates (Morkoç and Özgür 2009). Although the wurtzite structure of ZnO is the thermodynamically stable structure under ambient conditions, another metastable crystal structure of ZnO is sphalerite (cubic zinc blende), in which Zn ions occupy the corners and face-centers of each unit cell and O ions occupy half of the available tetrahedral sites (or vice versa).

Common neighbor analysis (Honeycutt 1987, Faken 1994) and polyhedral template matching (Larsen 2016) are commonly used for identification of simple crystal structures such as hexagonal close-packed and simple face-centered and body-centered cubic, but they cannot identify more complicated structures such as wurtzite and sphalerite. Wurtzite and hexagonal

Table 1. Number of ions in each NP-substrate system.

NP diameter (nm)	Total ions	NP ions	Substrate ions
10	486 680	43 160	443 520
20	3 893 292	345 132	3 548 160
30	13 140 023	1 164 983	11 975 040

diamond lonsdaleite have related structures; in lonsdaleite all ion positions present in wurtzite are occupied by carbon atoms rather than cations and anions. Sphalerite and cubic diamond also have related structures; in cubic diamond all ion positions present in sphalerite are occupied by carbon atoms rather than cations and anions. Because of the similarities between the two hexagonal structures and between the two cubic structures, differences between the wurtzite and sphalerite structures can be assessed using the 'Identify Diamond' tool in OVITO (Identify diamond structure, OVITO User Manual, Version 3.9.1). This tool was therefore used to identify phase transformation from the original wurtzite lattice.

Ions identified as cubic and hexagonal diamond indicate that all first and second nearest neighbors are positioned on cubic and hexagonal diamond lattice sites, respectively. Cubic diamond (1st neighbor) indicates the nearest neighbor of an ion was identified as cubic diamond. Cubic diamond (2nd neighbor) indicates the second nearest neighbor of an ion was identified as cubic diamond. The same explanation is also valid for hexagonal diamond (1st neighbor) and hexagonal diamond (2nd neighbor). Full methods for structure identification through this tool are outlined in Appendix A of the paper by Maras *et al* (2016) and in the OVITO User Manual.

2.3. Temperature calculation

Temperatures were calculated in LAMMPS with the 'compute temp' command by using the equation $T = \frac{2}{3} \times \frac{KE}{k_B}$, where KE corresponds to each atom's kinetic energy and k_B is the Boltzmann constant (Compute temp command 2023, LAMMPS Documentation, Version 15 June 2023). Per the LAMMPS documentation, temperatures are calculated from the prior equation after subtracting out 'degrees-of-freedom due to fixes that constrain molecular motion' and extraneous factors such as non-zero center-of-mass velocity, which can lead to misinterpretation of the overall kinetic energy (and thus temperature) over the course of a simulation. Reported temperatures are after spatial averaging within a radius of 0.5 nm ($0.05 \times d_{NP},\ 0.025 \times d_{NP}, 0.0167 \times d_{NP}$, respectively, for the 10 nm, 20 nm, and 30 nm NPs).

2.4. Simulation setup

At the onset of the simulation, the *x*-, *y*-, and *z*-directions in the substrate corresponded to the [210], [010], and [001] crystallographic directions, respectively. A spherical region of wurtzite lattice points was filled with Zn and O ions. The region was then thermalized at 300 K to relax the surface irregularities and allow the lattice constant to equilibrate in the bulk. The number of ions in the NP and substrate for each particle size are shown in table 1. The ZnO NP was rotated 45° about the vertical *c*-axis relative to the substrate to prevent immediate epitaxy between the NP and substrate upon impact.

Periodic boundaries were applied to all faces of the simulation box and a substrate of dimensions $2.35 \times d_{NP},\ 2.35 \times d_{NP}, 1.25 \times d_{NP}$ (in *x, y, z*) was placed in the bottom of the box, where d_{NP} denotes the diameter of the NP. The specified boundary conditions were chosen to approximate a semi-infinite substrate.

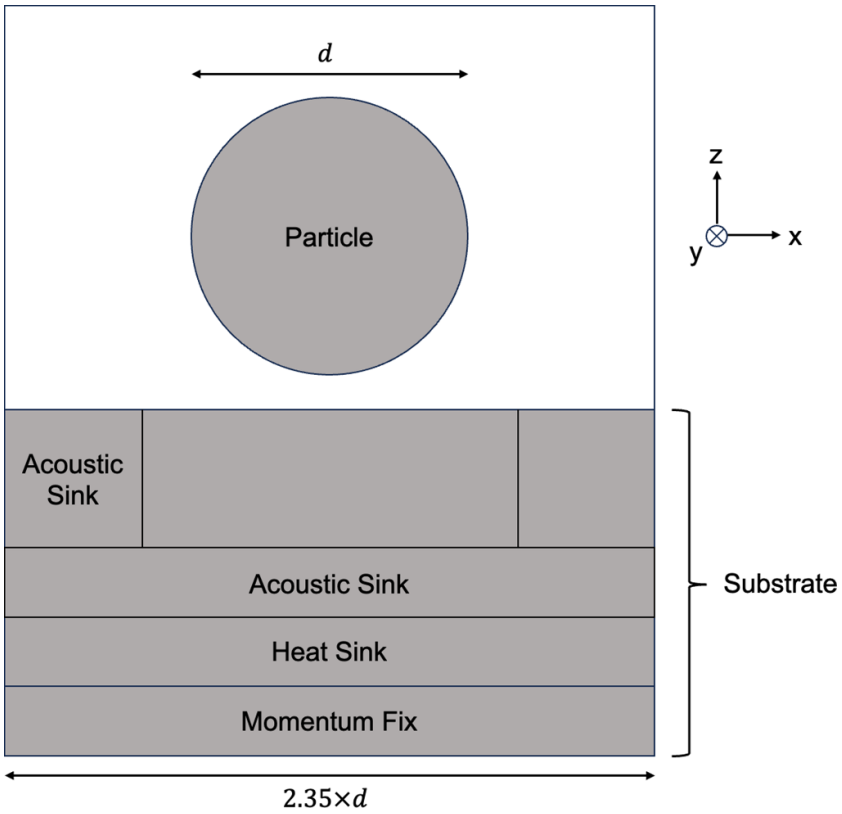

Figure 1. A schematic of the simulation box, nanoparticle, substrate, and applied boundary conditions.

Ions in the lower fifth of the substrate in the z-direction were assigned zero linear z-momentum at each timestep to prevent a net velocity of the substrate from the impacting NP. A heat sink was specified between the lower 1/5 and 2/5 of atoms in the substrate and assigned a temperature of 300 K to mimic heat conduction into a semi-infinite substrate. The 'fix temp/rescale' command in LAMMPS was used to ensure the heat sink remained at 300 K every timestep. Additionally, a Langevin acoustic sink was specified between the lower 2/5 and 3/5 of atoms in the substrate to prevent shockwaves from propagating through the periodic boundaries of the simulation box. Another Langevin acoustic sink was applied in an annular region between the region surrounding the impact area of the particle and the edges of the substrate. Both acoustic sinks were assigned a temperature of 300 K, with a damping parameter of 1 ps. A schematic of the simulation box, NP, substrate, and applied boundary conditions is shown in figure 1.

Before setting the particle in motion, the NP-substrate system was thermalized for 50 ps at 300 K and zero pressure by using an isothermal-isobaric (NPT) ensemble integrator with a thermal damping parameter of 0.1 ps and a pressure damping parameter of 1 ps (Moyers *et al* 2022, Davies *et al* 2022). Rotation of the NP was prevented during thermalization by assigning zero angular velocity. The NPT ensemble integrator was removed after equilibration to 300 K and replaced with a microcanonical (NVE) ensemble integrator before impact to update individual atom positions and velocities for each timestep. The impact portion of the simulation

was performed for 30 ps or 50 ps depending on NP diameter. These times were chosen because large scale changes in the configurations of the ions stabilized after between 5 ps and 15 ps. A timestep of 10^{-4} ps $= 10^{-1}$ fs was found to provide convergence for both the thermalization and deposition portions of the simulation. The default velocity-Verlet algorithm in LAMMPS for time-step integration was used (4.7. How a timestep works, LAMMPS Documentation, Version 15 June 2023). Simulation results were output to a text file every 10 000 timesteps (every 1 ps). OVITO was used to visualize the output data, including atom positions, atomic strain, potential energy, and temperature (Stukowski 2009).

2.5. Study parameters

Independent variables for this study include (1) particle diameter and (2) particle impact velocity. Our objectives were: to observe the relationships between particle size, impact velocity, and impact deformation mechanisms and to compare the impact behavior of mixed ionic-covalent ZnO to the behavior of previously studied ionic and covalent ceramic materials. NP impact angle was normal to the substrate surface for all simulations. Experiments have shown that deposition of ceramic particles occurs at velocities between 100 m s^{-1} and 500 m s^{-1} for particles larger than 100 nm (Akedo 2006, Hanft *et al* 2015). Preliminary simulations of individual 10–30 nm ZnO NPs within this range of impact velocities resulted in elastic bounce-off of the NP (no sticking or adhesion of the NP to the substrate). Particle impact velocities for the simulations were therefore increased incrementally by 500 m s^{-1} until a range of suitable impact velocities for sticking was determined; this occurred for impact velocities of between 1500 m s^{-1} and 3000 m s^{-1}. Due to the high velocity of the impact, non-adhering particles rebound and immediately leave the substrate. This allows sticking to be readily assessed from observation.

2.6. Calculation of amorphization and atomic strain

To assess the local deformation upon impact, the degree of amorphization within each NP, the local, cumulative volumetric strains, $(\varepsilon_{11} + \varepsilon_{22} + \varepsilon_{33})/3$, and the von Mises equivalent shear strain were assessed using OVITO. The reported strains were calculated instantaneously at each ion by spatial averaging within a radius of 0.5 nm for each timestep with reference to the initial, undeformed simulation cell.

2.7. Critical potential energy for ionic disordering

In prior MD studies pertaining to the high strain rate disordering of metals and ceramics, it has been proposed that the potential energy/ion (PE/Ion) can be used to predict when disordering of individual ions will occur (Becker and Kovar 2021, Chitrakar *et al* 2022, Moyers *et al* 2022). An ion reaching or exceeding the critical PE/Ion indicates that this ion will disorder. Such a criterion allows for the quantification of disordering independent of whether the disordering occurs in the solid state (amorphization) or liquid state (melting). Independent simulations on a cube of ZnO with dimensions $20 \times 20 \times 20$ lattice constants predicted a melting temperature of approximately 2000 K and a PE/Ion at this temperature of -3.4 eV for the ZnO potential used in this study (Erhart *et al* 2006). The critical PE/atom for disordering was therefore be taken to be -3.4 eV.

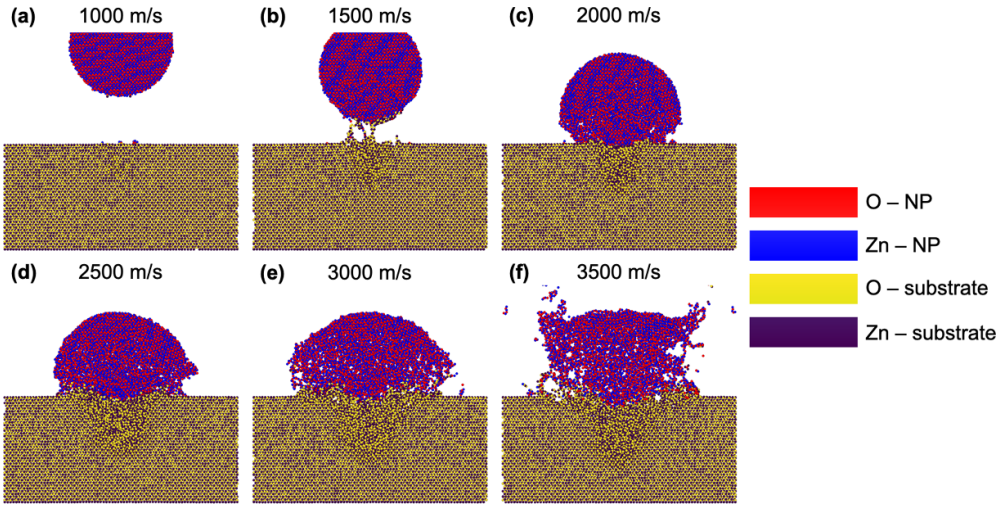

Figure 2. Prototypical impact behavior of a 10 nm diameter ZnO NP 20 ps after impact for impact velocities of (a) 1000 m s^{-1}, (b) 1500 m s^{-1}, (c) 2000 m s^{-1}, (d) 2500 m s^{-1}, (e) 3000 m s^{-1}, and (f) 3500 m s^{-1}. Zn ions are shown in purple and blue for the substrate and NP, respectively; O ions are shown in yellow and red for the substrate and NP, respectively. Images are of a center slice of the system with a thickness of four lattice constants (1.3 nm).

3. Results

3.1. NP impact behavior

Figure 2 shows prototypical impact behavior of a 10 nm diameter ZnO NP at impact velocities of 1000, 1500, 2000, 2500, 3000, and 3500 m s^{-1}. This figure shows that an impact velocity of 1500 m s^{-1} results in elastic rebound of the NP with only a few atoms from the particle remaining on the substrate. Impact velocities between 2000 and 3000 m s^{-1} result in desirable adhesion of the NP to the substrate. Increasing impact velocity within the range of velocities that results in adhesion causes an increase in global deformation experienced by the particle. Impact velocities greater than 3000 m s^{-1} result in damage to the NP with loss of many of the ions and significant amorphization of the substrate in the impact region.

Additional simulations were then performed for particle sizes of 20 nm and 30 nm. The global NP impact behaviors as a function of size for particles from 10 to 30 nm and impact velocities of 500–3500 m s^{-1} are summarized in table 2. This table shows that increasing particle size decreases the impact velocity necessary for adhesion, but also decreases the impact velocity at which extensive particle damage occurs upon impact. The remainder of figures shown in this paper (excluding figure 8) are at an impact velocity of 2000 m s^{-1}, as this value resulted in adhesion across all tested particle sizes.

3.2. Amorphization and atomic strain

Figure 3 shows results from simulations for 10, 20, and 30 nm NPs impacting at 2000 m s^{-1} at times of 1, 5, 10, and 20 ps after impact. The figure is color-coded by the identified crystal structure.

Table 2. NP impact behavior as a function of size and velocity.

NP diameter (nm)	Impact velocity (m s^{-1})	Impact behavior
10	<2000	Elastic bounce-off
10	$2000 \leqslant v \leqslant 3000$	Adhesion
10	>3000	Particle damage
20, 30	<1500	Elastic bounce-off
20, 30	$1500 \leqslant v \leqslant 2500$	Adhesion
20, 30	>2500	Particle damage

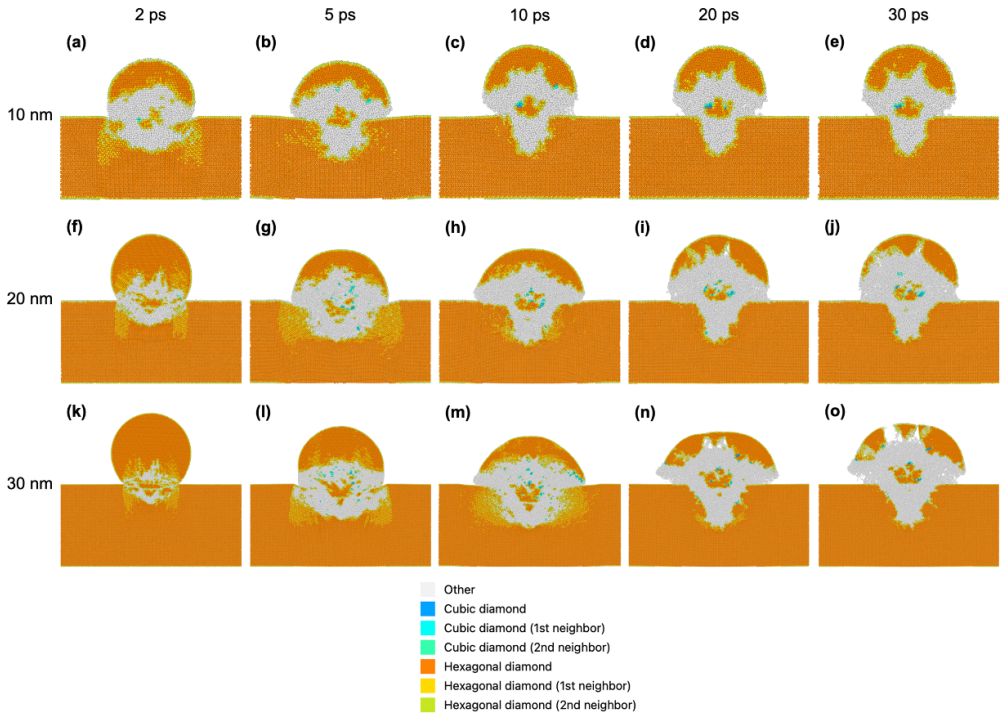

Figure 3. Results from simulations showing snapshots after particle impact for 10 (top row), 20 (middle row), and 30 nm (bottom row) particles. Ions are color coded to indicate the local crystal structure. Times are shown 2 ps, 5 ps, 10 ps, and 20 ps, and 30 ps after impact for ZnO NPs for an impact velocity of 2000 m s^{-1}. Images are of a center slice of the system with a thickness of four lattice constants (1.3 nm).

The impact behavior for the 10 nm NP is shown in figures 3(a)–(e). Elastic deformation and recoverable amorphization within both the NP and substrate occur immediately after impact (figure 3(a)). Approximately 5 ps after impact (figure 3(b)), the NP continues to move downward while maxima for both aspect ratio and degree of amorphization occur. The NP begins to rebound shortly thereafter and continues to do so until approximately 10 ps (figure 3(c)) after impact. However, by this time, the degree of amorphization within the particle has reached a steady state. By 20 ps (figure 3(d)), the NP has ceased movement and there are only short-range changes in ionic positions.

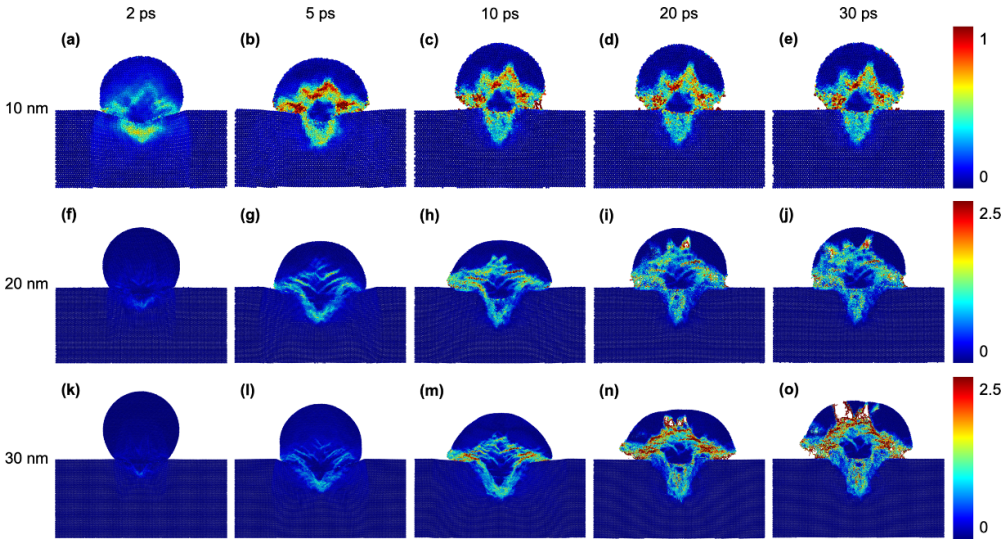

Figure 4. The von Mises equivalent shear strains 2 ps, 5 ps, 10 ps, 20 ps, and 30 ps after impact for ZnO NPs of diameter (a)–(e) 10 nm, (f)–(j) 20 nm, and (k)–(o) 30 nm at an impact velocity of 2000 m s^{-1}. Images are of a center slice of the system with a thickness of four lattice constants (1.3 nm).

Behavior that is very similar to the 10 nm case is observed on a larger scale for both the 20 and 30 nm NPs. However, the observed responses are delayed as particle size increases. The 20 nm NP case is shown in figures 3(f)–(j). At 5 ps after impact, the 20 nm NP is still moving downward and has not yet reached a maximum degree of amorphization (figure 3(g)). Approximately 10 ps after impact, the 20 nm NP experiences maximum amorphization and aspect ratio and begins to rebound (figure 3(h)). By 20 ps, the NP has stopped moving (figure 3(i)). The 20 nm NP has undergone more damage than the 10 nm NP, as indicated by the top, structured section of the 20 nm NP beginning to peel away from the large amorphous region. Furthermore, a larger change in NP aspect ratio and more ions in the NP-substrate contact region are observed in the final state of the 20 nm NP compared to the 10 nm NP (figure 3(j)). Similar phenomena are observed for the 30 nm NP in figures 3(k)–(o); compared to the smaller particles, impact events are delayed further, the final aspect ratio is noticeably larger, and more damage is apparent in the crystalline region near the top of the NP.

Figures 4 and 5 show 10, 20, and 30 nm NPs impacting at 2000 m s^{-1} at times of 2, 5, 10, 20, and 30 ps after impact and are color-coded by volumetric and shear strain in OVITO, respectively. Volumetric and shear strains for the 10 nm NP case are shown in figures 4 and 5(a)–(e). Elastic deformation begins to occur immediately after impact and the onset of strain is observed in the NP-substrate contact region (figures 4 and 5(a)). By 5 ps, localized areas of large shear and volumetric strain are observed immediately around the edges of the impact region and near the center of the NP (figures 4 and 5(b)). As the particle rebounds around 10 ps, areas of high strain have localized immediately around the crystalline region above the NP-substrate contact region (figures 4 and 5(c)). At 20 ps and 30 ps, the NP has ceased movement and the observed strain states are practically identical to those at 10 ps (figures 4 and 5(d), (e)).

Similar to the amorphization behavior in figure 3, observed phenomena are delayed as particle size increases. Volumetric and shear strains for the 20 nm NP are shown in figures 4

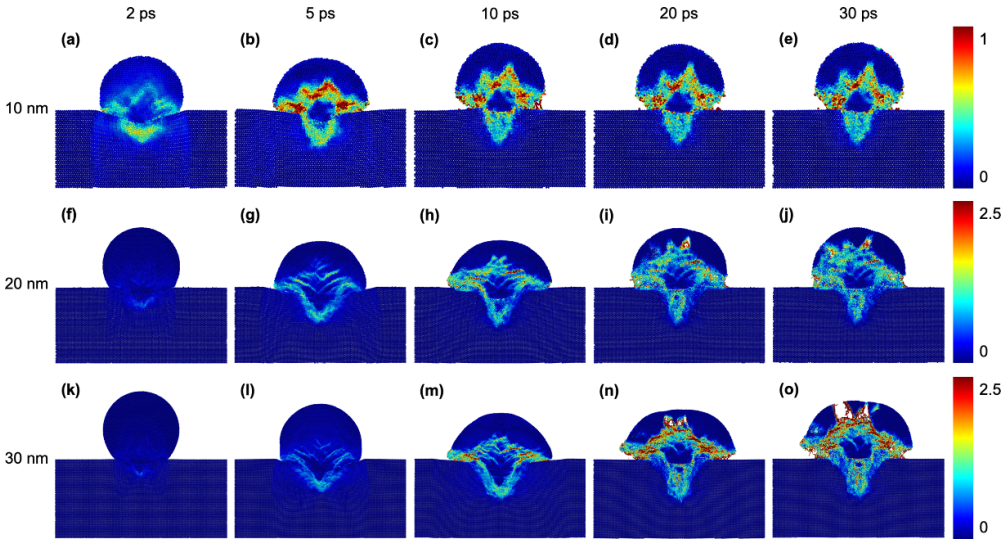

Figure 5. Volumetric strain 2 ps, 5 ps, 10 ps, 20 ps, and 30 ps after impact for ZnO NPs of diameter (a)–(e) 10 nm, (f)–(j) 20 nm, and (k)–(o) 30 nm at an impact velocity of 2000 m s^{-1}. Images are of a center slice of the system with a thickness of four lattice constants (1.3 nm).

and 5(f)–(j). There is essentially no strain present immediately after impact in the NP or substrate (figures 4 and 5(f)). By 5 ps, bands of low strain have begun to appear in both the NP and substrate around the area of impact (figures 4 and 5(g)). Approximately 10 ps after impact, the NP begins to rebound, and as observed in the 10 nm NP, areas of increased strain are localized around the edges of the impact region and near the center of the NP (figures 4 and 5(h)). However, unlike the 10 nm NP, localized pockets of increased strain are not apparent; that is, the both the volumetric and shear strains are nearly uniform throughout the bands of amorphous regions. This is apparent in figures 4 and 5(i), (j) when the NP has ceased movement.

Similar behavior to the 20 nm NP is observed for the 30 nm NP in figures 4 and 5(k)–(o) on a larger scale. As expected, the onset of large strains and the formation of localized shear bands are further delayed. However, the final strain state is more like the 10 nm NP than the 20 nm NP; distinguishable areas of high strain are apparent in the final state (figures 4 and 5(o)), which are not seen for the 20 nm NP. Interestingly, it is apparent that regions of low and high strain for all tested cases correspond to crystalline and amorphous regions, respectively, as identified in figure 3. Thus, there is a significant correlation between regions that amorphized and those regions with high volumetric and shear strain.

3.3. PE/Ion

Figure 6 shows results from simulations for 10, 20, and 30 nm NPs impacting at 2000 m s^{-1} at times of 2, 5, 10, 20, and 30 ps after impact. The figure is color-coded by PE/Ion. As discussed in section 2.7, the critical PE/Ion for ionic disordering was determined to be approximately −3.4 eV. To display this critical PE/atom, the color scale in figure 6 is set so that all ions with a PE/atom $\geqslant -3.4$ eV are shown in deep, saturated red.

PE/Ion for the 10 nm NP is shown in figures 6(a)–(e). Ions within the NP surpass the critical PE/Ion as soon as 2 ps after impact (figure 6(a)) and there is already a clear spatial similarity

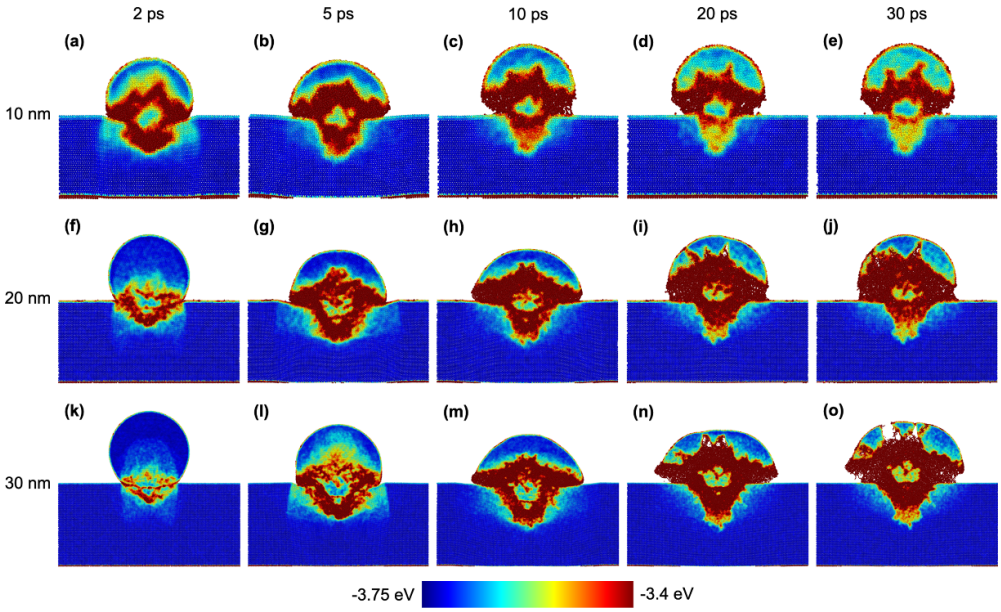

Figure 6. PE/Ion 2 ps, 5 ps, 10 ps, 20, and 30 ps after impact for ZnO particles of diameter (a)–(e) 10 nm, (f)–(j) 20 nm, and (k)–(o) 30 nm at an impact velocity of 2000 m s^{-1}. Images are of a center slice of the system with a thickness of four lattice constants (1.3 nm).

between this criterion and the identified crystal structure in figure 3(a). The amorphous region in the NP continues to grow as downward motion of the NP continues (figure 6(b)). As the particle approaches a steady state (figure 6(c)), the region of ions exceeding the critical PE/Ion has stabilized. By 20 and 30 ps (figures 6(d) and (e)), the NP has stabilized, and the amorphous regions still match with the above-threshold regions.

Similar behavior is observed for the 20 and 30 nm NPs. Numerous ions in the NP-substrate contact region have exceeded the PE/Ion threshold by 2 ps (figures 6(f) and (k)), although the above-threshold fraction is smaller compared to the 10 nm NP. Spatial similarity is observed with the both the amorphous regions and high-strain regions in figures 3–5(f) and (k). The number of ions exceeding −3.4 eV quickly grows for both the 20 and 30 nm NPs as each particle begins to rebound and eventually settle. Comparison to figure 3 shows spatial correspondence between ions which were identified as amorphous and those ions above the critical PE/Ion.

3.4. Temperature

Figure 7 shows results from simulations for 10, 20, and 30 nm NPs impacting at 2000 m s^{-1} at times of 2, 5, 10, 20, and 30 ps after impact. The figure is color-coded by temperature with the melting temperature as determined by the Erhart potential (∼2000 K) coded as deep red. For all cases, figure 7 shows that a small fraction of ions within both the NP and substrate reach the melting temperature, and these ions are concentrated immediately around the area of impact.

Figures 7(a)–(e) illustrate local temperatures for the 10 nm NP case. Similar to the observations of amorphization, an increase in temperature in the impact region is apparent immediately after impact (figure 7(a)). Localized pockets of ions near the bottom of the NP reach

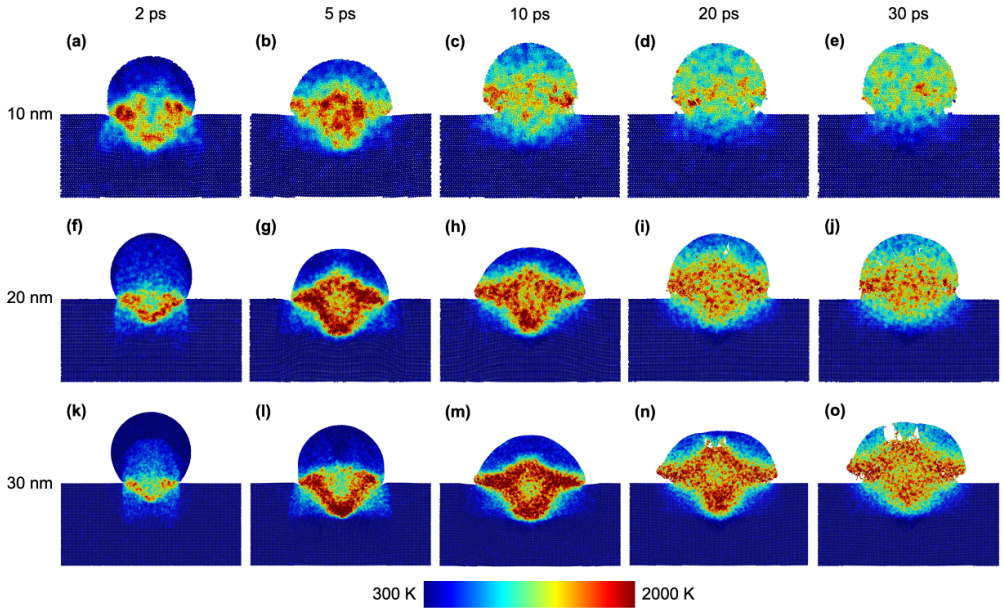

Figure 7. Temperature distributions 2 ps, 5 ps, 10 ps, 20, and 30 ps after impact for ZnO particles of diameter (a)–(e) 10 nm, (f)–(j) 20 nm, and (k)–(o) 30 nm at an impact velocity of 2000 m s^{-1}. Images are of a center slice of the system with a thickness of four lattice constants (1.3 nm).

2000 K, as quickly as 5 ps after impact (figure 7(b)). By 10 ps, most of the ions previously at or above 2000 K have decreased in temperature significantly; essentially all of the remaining ions that have reached 2000 K are concentrated on the bottom outer edges of the NP above the substrate (figure 7(c)). By 20 ps, the NP has ceased movement and most of the ions have cooled to approximately 1200 K (figure 7(d)). Unlike the regions of amorphization and high volumetric strain, which remain mostly in the lower ∼3/4 of the NP in the final state, local temperatures increase above 300 K in the entire NP. However, the temperature quickly drops back to ∼300 K in the substrate due to conduction.

Local temperatures for the 20 nm NP are shown in figures 7(f)–(j). Like the 10 nm NP, a temperature increase is apparent immediately after impact (figure 7(f)). However, unlike the 10 nm case, a small layer of high temperature ions is present as soon as 2 ps after impact that is localized at the edges of the NP-substrate contact region. The high temperature layer in the NP-substrate contact region quickly grows and encompasses the bottom of the NP by 5 ps (figure 7(g)). As the NP begins rebounding at approximately 10 ps after impact, the layer of high temperature ions has spread further, and the top of the NP begins to increase in temperature (figure 7(h)). At 20 ps and 30 ps, only a remnant of the continuous high temperature layer remains (figures 7(i) and (j)). Unlike the 10 nm case, the region immediately below impact in the substrate has also experienced a slight increase in temperature.

While temperature behavior of the 30 nm NP is similar to the 20 nm case, the delay in impact phenomena allows for better observation of the temperature evolution in the NP. A small layer of high-temperature ions is present in the NP-substrate contact region immediately after impact (figure 7(k)). By 5 ps after impact, the layer of high temperature ions evolves into a ‘V’ shape around the bottom outer edge of the NP (figure 7(l)). In figures 7(m)–(o), high

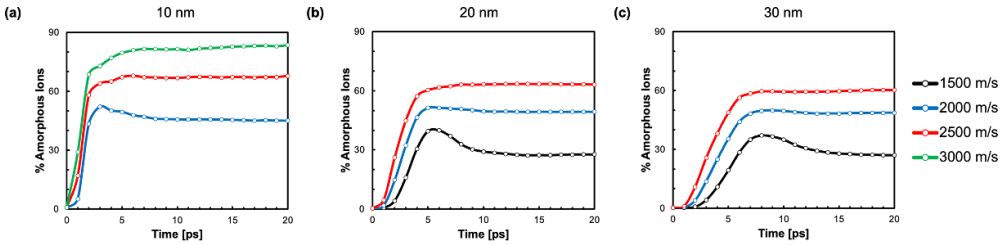

Figure 8. Plots of percent of amorphous NP ions as a function of time and impact velocity for NPs of diameter (a) 10 nm, (b) 20 nm, and (c) 30 nm. Only results for particle velocities where particle sticking occurred without particle destruction are shown.

temperature ions surround a central, crystalline region in which the ions have low temperature and low strain. A similar but less distinct central region is seen for the 20 nm NP by 10 ps in figures 7(g)–(i). As the NP rebounds and eventually reaches a final state, similar behavior is observed as in the 10 and 20 nm cases, yet more ions in the substrate immediately under the impact region experience a slight temperature increase (figures 7(n) and (o)). As noted for the 20 nm NP, regions of elevated temperature in the NP coincide with regions of amorphization and high strain early during impact, yet correspondence between such regions becomes less clear at longer times as thermal diffusion proceeds. Figure 7 shows that the magnitude of the temperature increase is larger and the temperature rise is also more localized as the particle size is increased.

3.5. Time dependence of amorphization

To further provide additional insight into the evolution of amorphization during and following impact, the percent of amorphous NP ions is plotted in figure 8 as a function of time and impact velocity.

Figure 8 illustrates the effect of impact velocity and diameter on amorphization within the NP. For all three particle sizes, particles impacted at the lowest velocity exhibit a rapid increase in percent ions amorphized and reach a peak before a fraction of the ions devitrify. This decrease in amorphized ions during devitrification is about 7% for the 10 nm particle, 12% for the 20 nm particle, and 10% for the 30 nm particle. At higher impact velocities, a similar rapid increase in percent ions amorphized is observed, but there is little devitrification apparent over the times scales of the simulations for any of the particle sizes. Furthermore, the time to amorphize ions decreases with impact velocity. For an impact velocity of 2000 m s^{-1}, the percent ions amorphized is between 45% and 50% for all three particle sizes and for an impact velocity of 2500 m s^{-1}, the percent atoms amorphized is between 60% and 67% for all three particle sizes. These plots show that the percent ions amorphized is relatively consistent among a range of particle sizes at a given impact velocity.

Notably, adhesion can be achieved with as low as approximately 27% of ions in the NP amorphizing. Thus, successful NP deposition at velocities in the lower end of the adhesion range indicates that plastic deformation via solid-state amorphization-induced viscous flow is the primary deformation mechanism present for this material.

4. Discussion

Discrepancies between experimentally reported impact velocities for particle adhesion and those reported in this paper are likely due to (1) particle morphology (i.e. experimental deposition of non-spherical particles and agglomerates versus individual spherical particles in MD simulations) and (2) particle size (MD-simulated particles being much smaller than those typically deposited experimentally). Furthermore, simulations are limited by available computational resources as the NP-substrate system can contain between hundreds of thousands and millions of ions, a majority of which are concentrated in the substrate. For the 10 nm NP system, the NP contained 43 160 ions and the substrate contained 443 520 ions; for the 20 nm NP system, the NP contained 345 132 ions and the substrate contained 3 548 160 ions; for the 30 nm NP system, the NP contained 1 164 983 ions and the substrate contained 11 975 040 ions.

In general, the NP undergoes elastic deformation within the first few ps of impact. If the specified impact velocity allows enough ions within the NP and substrate to dissipate energy via plastic flow, the NP will adhere to the substrate without eventually detaching. For ZnO, the plastic deformation primarily occurs by amorphization followed by viscous flow. Plastic deformation of both the NP and substrate occur simultaneously before reaching a mechanical steady state with only short-range changes in ion positions, temperature, PE/ion, and strain. Increasing NP diameter results in a delay of impact phenomena and increase in the NP settling time, i.e. the time necessary for the NP to reach a steady state after adhering to the substrate. This is especially apparent in figures 3–7; at an impact velocity of 2000 m s^{-1}, the 10 nm NP has settled approximately 10 ps into impact, 20 ps for the 20 nm NP, and 30 ps for the 30 nm NP. Furthermore, increases in both strain and amorphization occur simultaneously, implying an intrinsic relationship between the two.

Interestingly, a strong correlation between PE/Ion and amorphization was also observed for all particle sizes. Comparison of amorphization and PE/Ion in figures 3 and 6, respectively, indicates a rise in PE/Ion precisely where amorphization occurs, as early as 2 ps after impact. Prior high strain rate studies of metallic silver proposed the criterion of a critical value of PE/Atom in which amorphization occurs if an atom exceeds such a value (Becker and Kovar 2021, Chitrakar *et al* 2022); it was shown that this criterion quantified amorphization reasonably well for both biaxial strain and single NP impact cases. Moyers *et al* also utilized the PE/Ion criterion in their work to quantify amorphization of yttria NPs, in which there was agreement between PE/Ion and atomic strain. However, a comprehensive study on the PE/Ion criterion that would validate this criterion for ionic and/or covalent ceramics has not yet been conducted.

Select areas of the NP experienced significant heating during impact and small pockets of ions exceeded temperatures of 2000 K, which was found to be the approximate disordering temperature of ZnO using the potential by Erhart *et al.* However, this does not consider NP size or pressure effects on melting temperature that result from elevated pressures experienced during particle impact. It has previously been shown that a fraction of atoms exceeds the nominal melting point of primarily covalent SiC during particle impact (Davies *et al* 2022). However, studies of primarily ionic ceramics, including yttria (Moyers *et al* 2022), zirconia (Ogawa 2005, 2006), and hydroxyapatite (Jami and Jabbarzadeh 2020), did not report local temperatures exceeding the nominal melting points of each respective material. Significant rises in temperature were not observed for the lowest impact velocities that resulted in adhesion for each NP size in this study, indicating that melting is not a necessary particle deformation

mechanism for film formation. Thus, results for mixed ionic-covalent ZnO agree with previous literature for both ionic and covalent materials in which solid-state amorphization-induced viscous flow was proposed to be the primary particle deformation mechanism responsible for film formation.

5. Conclusions

MD simulations of a single ZnO NP impacting a ZnO substrate were performed by systematically varying particle diameter and impact velocity to determine their effects on the mechanisms responsible for film formation during MCS. Results of this study suggest that a narrow range of impact velocities exists in which ZnO NPs in the range of 10–30 nm can be successfully deposited, namely 2000–3000 m s^{-1} for a 10 nm NP and 1500–2500 m s^{-1} for 20 and 30 nm NPs. If using an impact velocity below or above this range, the NP will bounce off the substrate or sublimate, respectively. Furthermore, increasing particle size shifts the adhesion range and reduces the impact velocity necessary for successful deposition.

Increasing impact velocity within the adhesion range results in higher localized temperatures, a greater extent of amorphization, and an increase in the deformation of the impacting particle. Furthermore, the time necessary for impact events to occur was found to be relatively independent of impact velocity while having a large dependence on particle size. The time necessary to reach maximum percent of amorphous atoms was found to depend on both particle size and impact velocity. Although elevated temperatures were observed in regions of the NPs, adhesion occurred without significant rises in temperature for the lowest velocity cases across all particle sizes. Such data suggests that solid-state amorphization and viscous flow can occur independently of melting and are the primary deformation mechanisms experienced within this particle size range.

Data availability statement

All data that support the findings of this study are included within the article (and any supplementary files).

Acknowledgments

We acknowledge fruitful conversations with Stephen Bierschenk (UT), Derek Davies (UT), and Aidan Moyers (LANL/UT) that helped contribute to the success of the simulations outlined in this paper. This work was funded by the National Science Foundation (NSF) under Grant No. CMMI 2102818. We acknowledge the Texas Advanced Computing Center (TACC) at the University of Texas at Austin for providing Stampede2 (Cray Linux HPC Cluster) resources that have contributed to the simulations and results outlined in this paper (www.tacc.utexas.edu/).

Conflict of interest

The authors declare that they have no known competing financial interests or personal relationships that could have appeared to influence the work reported in this paper.

ORCID iDs

Scott Burlison https://orcid.org/0000-0003-1761-9099
Michael F Becker https://orcid.org/0000-0003-2992-9756
Desiderio Kovar https://orcid.org/0000-0002-1810-7653

References

4.7. How a timestep works *Lammps.org.* (available at: https://docs.lammps.org/Developer_flow.html) (Accessed 5 July 2023)
Akedo J 2006 Aerosol deposition of ceramic thick films at room temperature: densification mechanism of ceramic layers *J. Am. Ceram. Soc.* **89** 1834–9
Akedo J 2008 Room temperature impact consolidation (RTIC) of fine ceramic powder by aerosol deposition method and applications to microdevices *J. Therm. Spray Technol.* **17** 181–98
Becker M F and Kovar D 2021 A quantitative criterion for predicting solid-state disordering during biaxial, high strain rate deformation *Model. Simul. Mater. Sci. Eng.* **30** 015006
Chitrakar T V, Becker M F and Kovar D 2022 A quantitative criterion to predict atomic disordering during high velocity nanoparticle impact *J. Aerosol. Sci.* **165** 106042
Compute temp command 2023 *Lammps.org* (available at: https://docs.lammps.org/compute_temp_com.html) (Accessed 20 July 2023)
Daneshian B, Gärtner F, Assadi H, Vidaller M V, Höche D and Klassen T 2022 Features of ceramic nanoparticle deformation in aerosol deposition explored by molecular dynamics simulation *Surf. Coat. Technol.* **429** 127886
Davies D W, Moyers A H, Gammage M D, Keto J W, Becker M F and Kovar D 2022 Deformation and film formation mechanisms during high velocity impact of silicon carbide nanoparticles *J. Aerosol. Sci.* **163** 105997
Erhart P, Juslin N, Goy O, Nordlund K, Müller R and Albe K 2006 Analytic bond-order potential for atomistic simulations of zinc oxide *J. Phys.: Condens. Matter* **18** 6585–605
Exner J, Linz M, Kita J and Moos R 2021 Making powder aerosol deposition accessible for small amounts: a novel and modular approach to produce dense ceramic films *Int. J. Appl. Ceram. Technol.* **18** 2178–96
Faken D and Jónsson H 1994 Systematic analysis of local atomic structure combined with 3D computer graphics *Comput. Mater. Sci.* **2** 279–86
Gheewala I 2010 Multiscale modelling of nanoindentation of multi-layered systems *Thesis* Loughborough University (available at: https://hdl.handle.net/2134/34987)
Gheewala I, Kenny S D and Smith R 2009 Atomistic-scale modelling of nanoindentation into optical coatings *Phil. Mag.* **89** 3499–510
Gibas A, Winnicki M, Baszczuk A and Jasiorski M 2023 Influence of spraying parameters on microstructure of oxygen-rich TiO_2 coatings deposited using suspension low-pressure cold spray *Surf. Coat. Technol.* **457** 129321
Hanft D, Bektas M and Moos R 2018 Powder pre-treatment for aerosol deposition of tin dioxide coatings for gas sensors *Materials* **11** 1342
Hanft D, Exner J, Schubert M, Stöcker T, Fuierer P and Moos R 2015 An overview of the aerosol deposition method: process fundamentals and new trends in materials applications *J. Ceram. Sci. Technol.* **6** 147–82
Honeycutt J D and Andersen H C 1987 Molecular dynamics study of melting and freezing of small Lennard-Jones clusters *J. Phys. Chem.* **91** 4950–63
Identify diamond structure *Ovito.org.* (available at: www.ovito.org/manual/reference/pipelines/modifiers/identify_diamond.html) (Accessed 14 May 2023)
Jami H and Jabbarzadeh A 2020 Ultrafast thermomechanical effects in aerosol deposition of hydroxyapatite nanoparticles on a titanium substrate *Surf. Coat. Technol.* **382** 125173
Kim K and Lee K 2019 Room temperature impact-induced deposition of pure SiC coating layer by vacuum kinetic spraying *J. Am. Ceram. Soc.* **103** 54–59
Klingshirn C 2007 ZnO: from basics towards applications *Basic Solid State Phys.* **244** 3027–73
Larsen P M, Schmidt S and Schiøtz J 2016 Robust structural identification via polyhedral template matching *Modelling Simul. Mater. Sci. Eng.* **24** 055007

Ma J, Becker M F, Keto J W and Kovar D 2010 Laser ablation of nanoparticles and nanoparticulate, thick $Fe_{1.92}Tb_{0.3}Dy_{0.7}$ films *J. Mater. Res.* **25** 1733–40
Maras E, Trushin O, Stukowski A, Ala-Nissila T and Jónsson H 2016 Global transition path search for dislocation formation in Ge on Si(001) *Comput. Phys. Commun.* **205** 13–21
McCallister J J H, Gammage M D, Keto J W, Becker M F and Kovar D 2021 Influence of agglomerate morphology on micro cold spray of Ag nanopowders *J. Aerosol Sci.* **151** 105648
McCallister J J H, Keto J W, Becker M F and Kovar D 2019 Influence of normal velocity on microstructure and density of films produced by nanoparticle impact *AIP Adv.* **9** 035226
Morkoç H and Özgür Ü 2009 Zinc oxide: fundamentals, materials and device technology (Wiley-VCH Verlag GmBH & Co.)
Moyers A H, Becker M F and Kovar D 2023 A strain density function to analyze particle size effects during high velocity impacts of yttria submitted
Moyers A H, Davies D W, Becker M F and Kovar D 2022 A molecular dynamics survey study of impact-induced amorphization in yttria nanoparticles *J. Aerosol Sci.* **162** 105976
Mulheran P A and Meskine H 2011 Simulation of reconstructions of the polar ZnO(0001) surfaces *Phys. Rev.* B **84** 165430
Ogawa H 2005 Molecular dynamics simulation on the single particle impacts in the aerosol deposition process *Mater. Trans.* **46** 1235–9
Ogawa H 2006 Atomistic simulation of the aerosol deposition method with zirconia nanoparticles *Mater. Trans.* **47** 1945–8
Plimpton S 1995 Fast parallel algorithms for short-range molecular dynamics *J. Comput. Phys.* **117** 1–19
Song G, Adamczyk J, Park Y, Toberer E S and Hogan C J 2021 Spray pyrolysis-aerosol deposition for the production of thick yttria-stabilized zirconia coatings *Adv. Eng. Mater.* **23** 2100255
Stukowski A 2009 Visualization and analysis of atomistic simulation data with OVITO—the open visualization tool *Modelling Simul. Mater. Sci. Eng.* **18** 015012
Tadmor E B, Elliott R S, Sethna J P, Miller R E and Becker C A 2011 The potential of atomistic simulations and the knowledgebase of interatomic models *J. Miner. Met. Mater. Soc.* **63** 17
Thompson A P *et al* 2022 LAMMPS—a flexible simulation tool for particle-based materials modeling at the atomic, meso, and continuum scales *Comput. Phys. Commun.* **271** 108171
Toe M Z, Tan W K, Muto H, Kawamura G, Matsuda A, Yaacob K A B and Pung S 2022 Effect of carrier gas flow rates on the structural and optical properties of ZnO films deposited using an aerosol deposition technique *Electron. Mater.* **3** 332–43